Supporting Information

Influence of Sequential Perovskite Deposition at the Self-Assembled Monolayer Interfaces in Inverted Perovskite Solar Cells

*Sua Park,[a] Donghyeon Lee,[a] Shinhyun Kim,[a] Pedro Roberto Mercado Lozano,[b] Sarah Wieghold,[b] Sayantan Mahapatra,[c] Soumyajit Rajak,[d] Nan Jiang,[de] Jeffrey R. Guest,[c] Yanqi Luo *[b] and Min-cheol Kim *[a]*

[a]*School of Mechanical Engineering, Pusan National University, Busan 46241, Republic of Korea*

[b]*Advanced Photon Source, Argonne National Laboratory, Lemont, Illinois 60439, United States*

[c]*Center for Nanoscale Materials, Argonne National Laboratory, Lemont, Illinois 60439, United States*

[d]*Department of Chemistry, University of Illinois Chicago, Chicago, Illinois 60607, United States*

[e]*Department of Physics, University of Illinois Chicago, Chicago, Illinois 60607, United States*

* Correspondences: yluo89@anl.gov (Y. Luo); mckim90@pusan.ac.kr (M.-c. Kim)

Experimental Section

Materials

Tin oxide (SnO_2 nanoparticle dispersion, 15% in H_2O colloidal, Alfa Aesar), poly(triaryl amine) (PTAA, Sigma-Aldrich), 9,9-bis(3-(N,N-dimethylamino)propyl)-2,7-fluorene)-alt-2,7-(9,9-dioctylfluorene) (PFN, Sigma-Aldrich), [2-(9H-Carbazol-9-yl)ethyl]phosphonic Acid (2PACz, 98%, TCI), [4-(7H-Dibenzo[c,g]carbazol-7-yl)butyl]phosphonic Acid (4PADCB, 98%, TCI), lead iodide (PbI_2, 99.99%, TCI), cesium iodide(CsI, 99.999%, Sigma-Aldrich), formamidinium iodide (FAI, 99.99%, Greatcellsolar), methylammonium chloride (MACl, 99.99%, Greatcellsolar), methylammonium bromide (MABr, 99.99%, Greatcellsolar), propylammonium chloride (PACl, 98.0%, TCI), 1,3-diaminopropane dihydroiodide ($PDAI_2$, 98%, TCI), lithium bis(trifluoromethane)sulfonimide (Li-TFSI, 99.95% Sigma-Aldrich), Tris[4-tert-butyl-2-(1H-pyrazol-1-yl)pyridine]cobalt(III) Tris(trifluoromethanesulfonyl)imide (FK209 Co(III) TFSI salt, Greatcellsolar), 2,2',7,7'-Tetrakis(N,N-di-p-methoxyphenylamino)-9,9'-spirobifluorene (Spiro-MeOTAD, 99%, Luminescence Technology Corp.), N,N-dimethyl formamide (DMF, 99%, Sigma-Aldrich), dimethyl sulfoxide (DMSO, 99%, Sigma-Aldrich), N-methyl-2-pyrrolidone (NMP, 99%, Sigma-Aldrich), oleylamine (OLA, >50.0%, TCI), 2-propanol (IPA, 99.5%, Sigma-Aldrich), ethanol (99%, Sigma-Aldrich), deionized water (99%, Alfa Aesar), toluene (99%, Sigma-Aldrich), chlorobenzene (CB, 99%, Sigma-Aldrich), methanol (99%, Sigma-Aldrich), acetonitrile (ACN, 99%, Sigma-Aldrich), 4-tert-butylpyridine (4-TBP, 98%, Sigma-Aldrich) were used as-received without further purifications.

Perovskite precursor preparation

For one-step perovskite (OP), the OP precursor solution was prepared by mixing 15 mg of MACl, 15mg of PACl, 46.8 mg of CsI, 278.6 mg of FAI, 864.4 mg of PbI_2 in 1 mL of DMF (added 1.6 mmol OLA)/NMP (4:1 v/v). For two-step perovskite (TP), 1.5 M of PbI_2 powder

was dissolved in DMF/DMFSO (9:1 v/v) and organic halide solution was prepared by mixing 9 mg of MABr, 9 mg of MACl, 90 mg of FAI in 1 mL of IPA. For mixed two-step perovskite (MP), the 2PACz powder was added to the PbI_2 solution used in the TP process, and the organic halide solution was kept the same as in TP.

Perovskite film fabrication

The OP precursor solution was spin coated at 5000 rpm for 8 s and subjected to vacuum-flash evaporation, and then annealed at 130 °C for 30 min. For the TP and MP precursor solution, the PbI_2 solution and the mixed 2PACz/PbI_2 solution was spin coated at 1600 rpm for 30 s and organic halide solution was spin coated at 2000 rpm for 30 s, and then annealed at 150 °C for 15 min.

Perovskite solar cells fabrication

The glass/ITO substrates (2.5 cm × 2.5 cm) were sequentially cleaned by sonication in acetone, isopropanol and deionized water for each 15 min and dried with nitrogen gas. Then the dry substrates treated with UV/Ozone for 15 min.

For n–i–p devices, the SnO_2 solution was mixed with deionized water (1:4 v/v) and the 180 μL of SnO_2 solution as electron transport layer (ETL) was spin coated on treated glass/ITO substrates at 4000 rpm for 30 s and annealed at 150 °C for 30 min. And the perovskite precursor was spin coated followed by OP and TP process. The Spiro-MeOTAD solution was prepared by dissolving 72 mg of Spiro-MeOTAD in 1 mL of CB and mixed with 28.8 μL of 4-TBP and 17.5 μL of Li-TFSI (520 mg/mL of ACN) and 11 μL of FK209 Co (III) TFSI (375 mg/mL of ACN). The 70 μL of Sprio-MeOTAD solution as hole transport layer (HTL) was spin coated at 2300 rpm for 30s with dynamic drop. The devices were completed by evaporating gold (50 nm).

For p–i–n devices, We used PTAA (5 mg/mL in CB) or 2PACz (1 mg/mL in ethanol) as HTL. For polymer-based HTL, The 150 μL of PTAA solution was spin coated on treated glass/ITO substrates at 5000 rpm for 30 s and annealed at 100 °C for 10 min. After that, the 100 μL of PFN solution (0.4 mg/mL in methanol) was spin coated at 4000 rpm for 20 s. For self-assembled monolayer (SAM) based HTL, The 150 μL of 2PACz solution was spin coated on treated glass/ITO substrates at 3000 rpm for 30 s and annealed at 100 °C for 10 min. The 150 μL of 4PADCB (0.5 mg/mL in ethanol) solution was spin coated on treated glass/ITO substrates at 4000 rpm for 30 s and annealed at 100 °C for 10 min. And the perovskite precursor was spin coated followed by OP, TP and MP process. The 1.5 mM of $PDAI_2$ was dissolved in toluene/IPA (1:1 v/v) for passivation layer and was spin coated at 3000 rpm for 30s with dynamic drop and annealed at 110 °C for 10 min. The devices were completed by sequentially thermally evaporating C_{60} (20 nm), BCP (6 nm) and gold (50 nm). All spin-coating processes were performed in a dry room with a relative humidity of less than 10% and a temperature of under 25 °C.

Characterization

For the device characterization, simulated AM1.5G irradiation (100 mW cm^{-2}) was produced using and Oriel Sol3A Class AAA solar simulator in a nitrogen-filled glove box. The device active area was 0.078 cm^2 and was masked with a metal aperture. The scanning electron microscopy (SEM) images were collected using a SUPRA25 microscope. X-ray diffraction (XRD) patterns were obtained using a PANalytical Xpert3 Materials Research Diffractometer system with a Cu Kα radiation source (λ = 1.540598 Å) operated at 40 kV and 30 mA. All diffraction patterns were measured at room temperature, with a step size of 0.026° and scan speed 0.32° s^{-1}. Atomic force microscopy (AFM) measurements were conducted using an XE-7 (Park Systems). X-ray photoelectron spectroscopy (XPS) was measured using the AXIS SUPRA XPS system (KRATOS Analytical Ltd.) with Al Kα X-ray radiation (1486.6 eV). The

steady-state photoluminescence (PL) and time-resolved PL (TRPL) was measured at room temperature using an FS5 spectrofluorometer (Edinburgh Instruments) with Xenon lamp source and pulsed laser excitation wavelength of 450 nm, respectively. The tip-enhanced Raman spectroscopy (TERS) was carried out in a variable temperature scanning tunneling microscopy (STM) system (USM1400, UNISOKU Co., Ltd.) and home-built TERS setup at liquid nitrogen temperature (78 K) under a base pressure of ~10^{-11} torr. Electrochemically etched silver (Ag) tips were used for STM-based TERS experiments. A 561 nm solid-state laser polarized parallel to the tip was utilized (incoming photon source) for the TERS experiments. For all the TERS measurements, laser power was 5.4 mW with an acquisition time of 60 s. The TERS signal was detected by an iso-plane SCT320 spectrograph (Princeton Instrument) combined with a Princeton Instrument PIXIS 100 CCD. The far-field Raman mapping was measured using an Ramantouch with an excitation laser wavelength of 532 nm and excitation power was 0.02 mW. The pixel size is 0.4 μm × 0.4 μm. The contact angle measurement was conducted Photron Nova S9 equipment with perovskite (for OP) or PbI_2 precursor solution (for TP, MP) dropping on the ITO/2PACz substrates. Stability measurements were performed under continuous light soaking under simulated AM1.5G irradiation in a nitrogen-filled glove box at room temperature, with PCE periodically extracted from *J–V* measurements over 400 h. The PCE values are normalized to the initial performance. Stability test for TP and MP devices has the structure glass/ITO/2PACz/perovskite/$PDAI_2$/C_{60}/BCP/Au and were encapsulated prior to testing.

Table S1. A summary of the bi-exponential fitting results for time-resolved photoluminescence data with different samples on ITO/SAM substrates.

Sample	A_1 (%)	A_2 (%)	τ_1 (ns)	τ_2 (ns)	τ_{avg} (ns)
ITO/SAM/OP	99.97	0.03	7.67	171.84	8.67
ITO/SAM/TP	92.17	7.83	19.71	628.02	463.97
ITO/SAM/MP	99.99	0.01	6.23	215.39	6.65

$$y = y_0 + A_1 e^{-x/\tau_1} + A_2 e^{-x/\tau_2} \quad (1)$$

$$\tau_{avg} = (A_1\tau_1^2 + A_2\tau_2^2)/(A_1\tau_1 + A_2\tau_2) \quad (2)$$

The bi-exponential decay function (Equation 1) is used, where A_1 and A_2 represent the decay amplitudes, and y_0 is a constant for baseline offset. The average lifetime (τ_{avg}) was calculated using the Equation 2.

TRPL measurements in Table S1 were performed on glass/ITO/SAM/perovskite half-cell, where photogenerated carriers can be quenched via charge transfer to the conductive ITO substrate in addition to recombination within the perovskite film. In this configuration, the TRPL decay is governed by a combination of interfacial carrier transfer/extraction and recombination pathways, and the bi-exponential fitting parameters should be regarded as effective time constants describing different temporal regimes rather than uniquely assigned microscopic mechanisms. The fast component (τ_1) primarily reflects early-time interfacial quenching process (carrier extraction and interfacial non-radiative loss), while the slow component (τ_2) represents the late-time decay of the remaining carrier population, which is influenced by bulk-interface recombination within the perovskite layer. Consequently, the extracted lifetimes are sensitive to the quality of the buried SAM/perovskite interface and the efficiency of interfacial carrier transfer.

Table S2. A summary of the bi-exponential fitting results for time-resolved photoluminescence data with different samples on glass/SAM substrates.

Sample	A_1 (%)	A_2 (%)	τ_1 (ns)	τ_2 (ns)	τ_{avg} (ns)
Glass/SAM/TP	68.51	31.49	22.96	365.95	324.75
Glass/SAM/MP	77.18	22.82	18.22	448.40	396.42

$$y = y_0 + A_1 e^{-x/\tau_1} + A_2 e^{-x/\tau_2} \quad (1)$$

$$\tau_{avg} = (A_1\tau_1^2 + A_2\tau_2^2)/(A_1\tau_1 + A_2\tau_2) \quad (2)$$

The bi-exponential decay function (Equation 1) is used, where A_1 and A_2 represent the decay amplitudes, and y_0 is a constant for baseline offset. The average lifetime (τ_{avg}) was calculated using the Equation 2.

TRPL measurements in Table S2 were conducted on glass/SAM/perovskite substrates without a conductive bottom electrode, thereby minimizing charge extraction pathways and allowing the decay to predominantly reflect recombination within the perovskite film. Similar to the half-cell case, the bi-exponential components are interpreted as effective time constants associated with distinct temporal regimes. The fast component (τ_1) captures early-time carrier loss processes that can include interface trapping and other rapid nonradiative pathways, while the slow component (τ_2) corresponds to the late-time decay governed by the effective recombination lifetime of the remaining carriers (often strongly influenced by trap-assisted non-radiative recombination under low-injection conditions). Accordingly, these measurements primarily probe bulk-limited recombination dynamics and defect passivation effects rather than interfacial charge extraction.

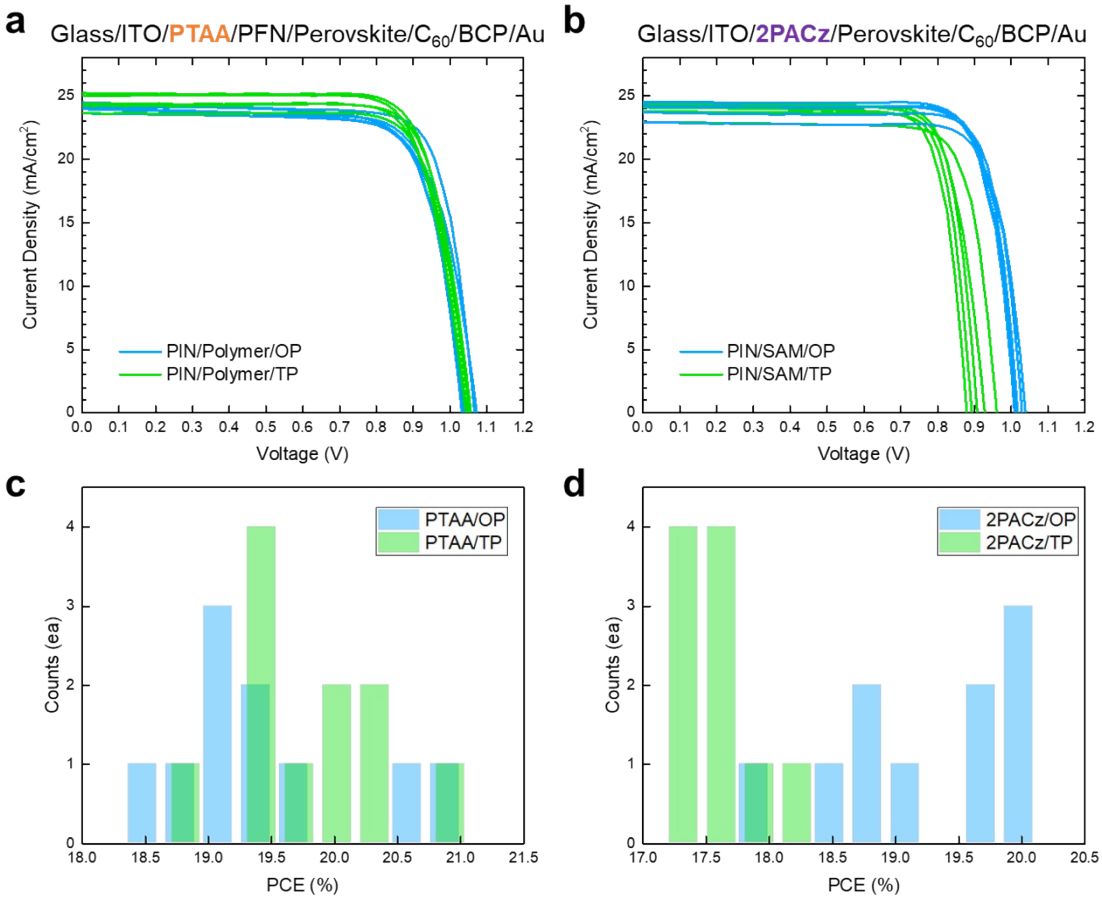

Figure S1. *J–V* curves of inverted PSCs using (a) PTAA/PFN and (b) 2PACz as the HTL fabricated by the OP and TP processes. PCE histograms of devices based on (c) PTAA/PFN and (d) 2PACz HTL.

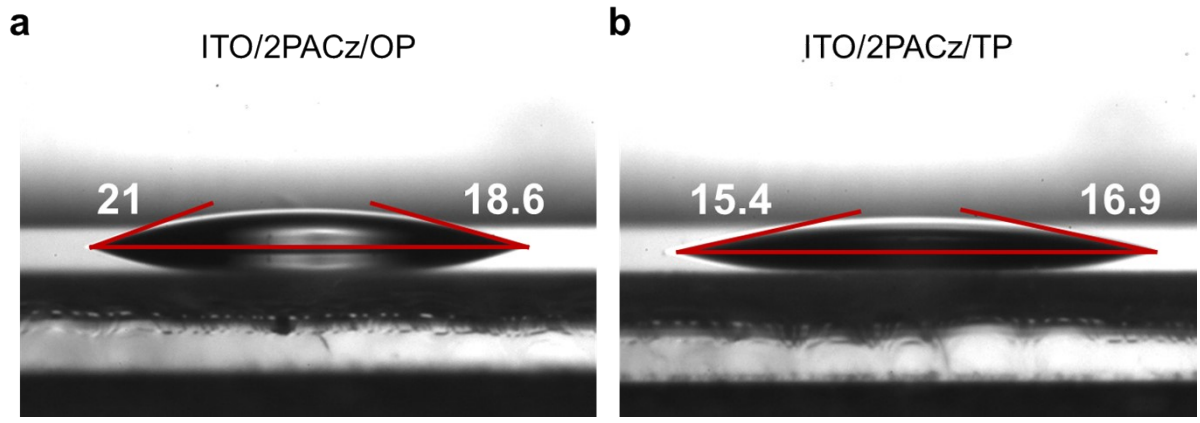

Figure S2. Contact angle measurement of (a) perovskite (OP) and (b) PbI_2 (TP) solution on same ITO/2PACz substrate.

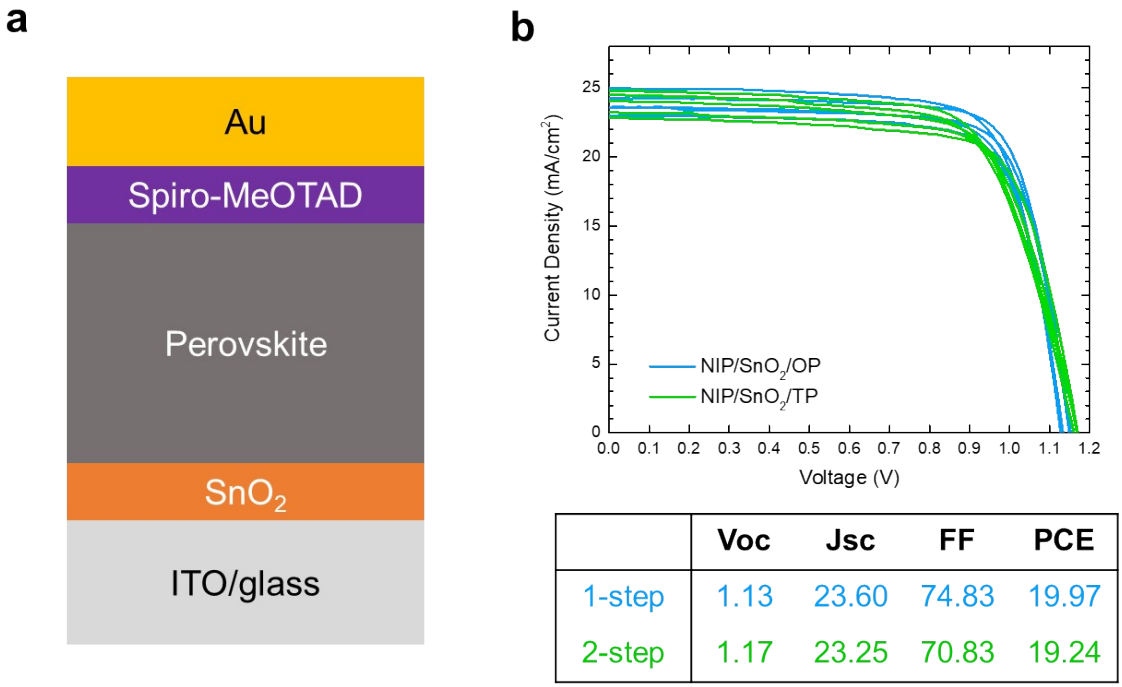

	Voc	Jsc	FF	PCE
1-step	1.13	23.60	74.83	19.97
2-step	1.17	23.25	70.83	19.24

Figure S3. (a) Schematic of n–i–p PSCs structure and (b) *J–V* curves of n–i–p PSCs fabricated by the OP and TP processes and its champion cells data.

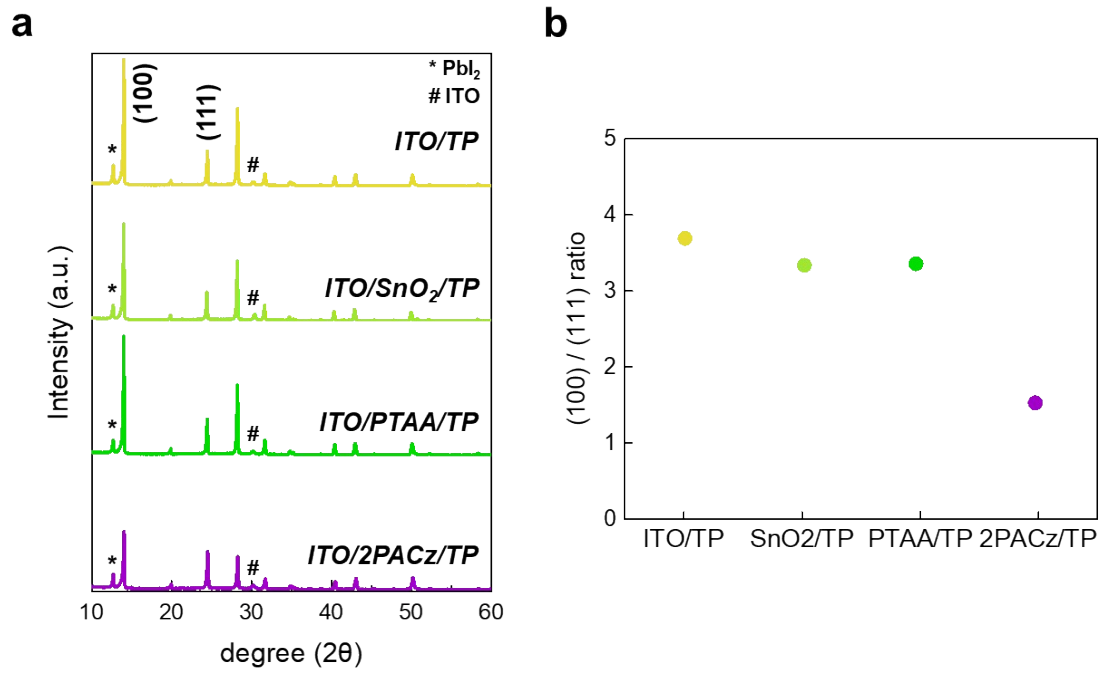

Figure S4. (a) XRD patterns of TP films deposited on different underlayers (ITO, ITO/SnO_2, ITO/PTAA, ITO/2PACz). (b) Corresponding intensity ratio of the (100) and (111) diffraction peaks.

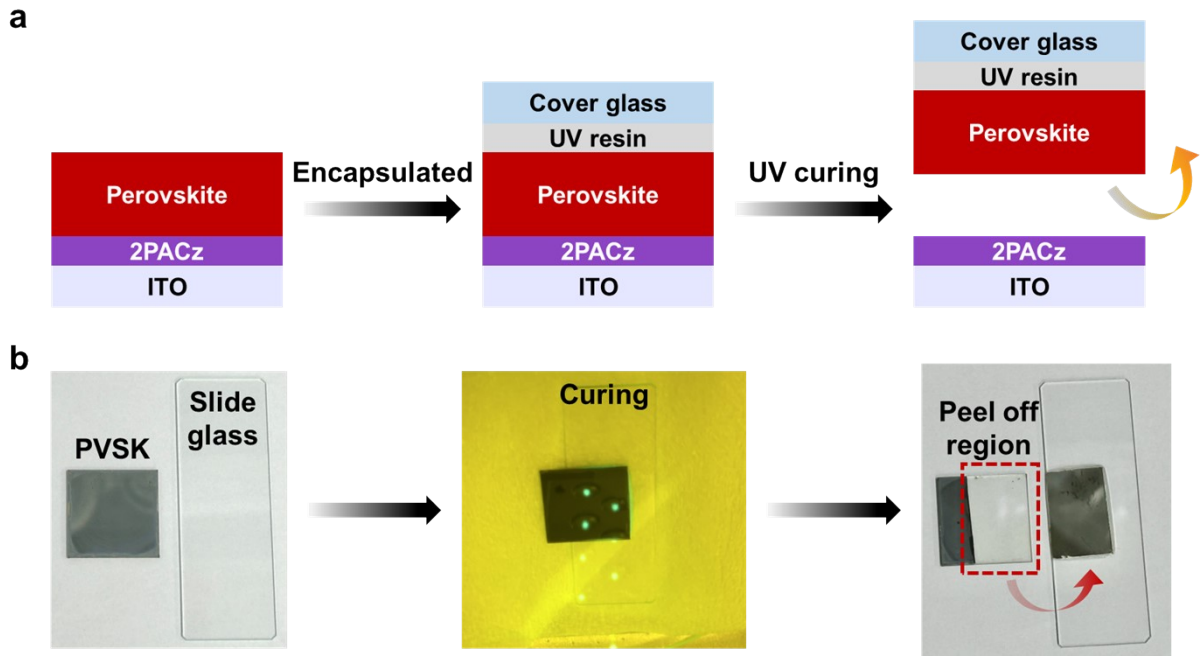

Figure S5. (a) Schematic illustration and (b) real images of peel-off process.

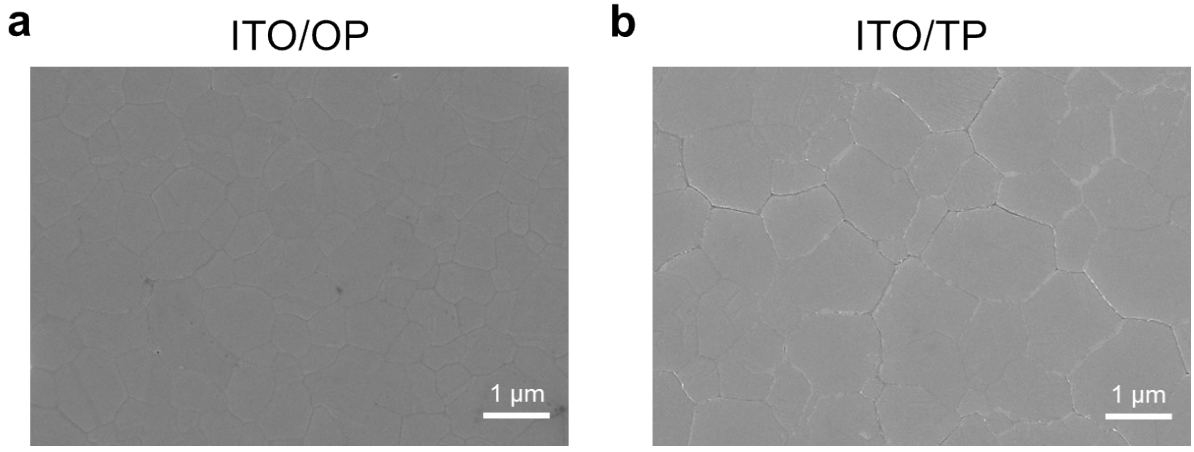

Figure S6. SEM images of the peel-off bottom perovskite surface for (a) ITO/OP and (b) ITO/TP. Scale bar: 1 μm.

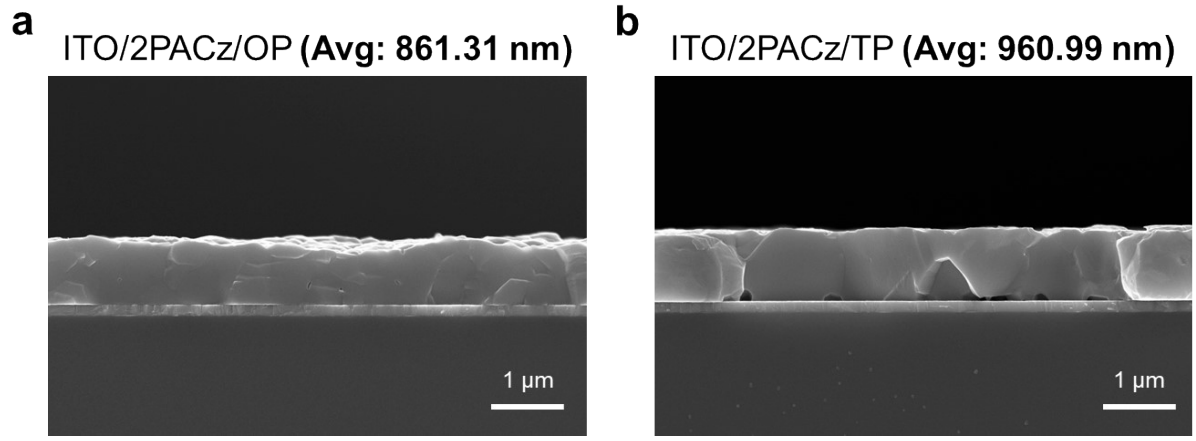

Figure S7. Cross-sectional SEM images of (a) ITO/2PACz/OP and (b) ITO/2PACz/TP. Scale bar: 1 μm.

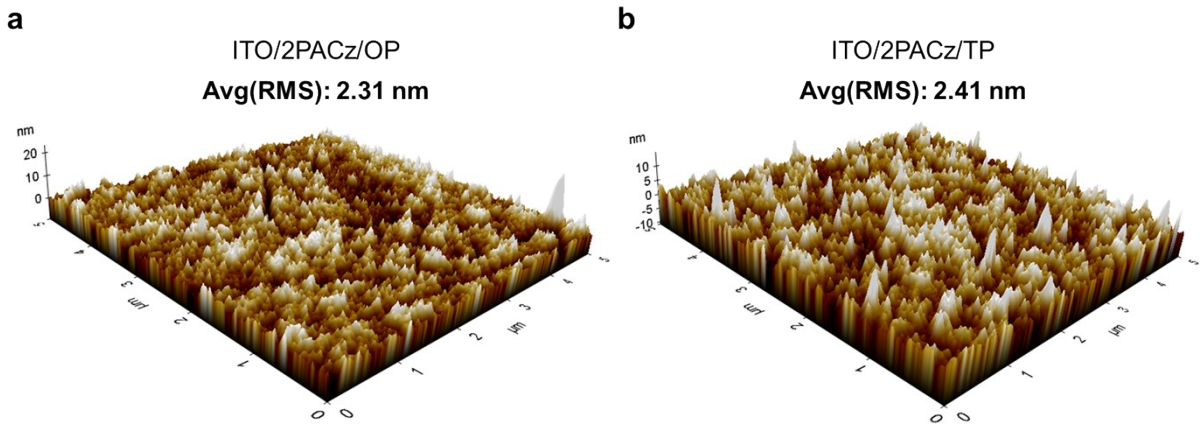

Figure S8. Three-Dimensional (3D) AFM images of peel-off SAM surface with (a) ITO/2PACz/OP and (b) ITO/2PACz/TP.

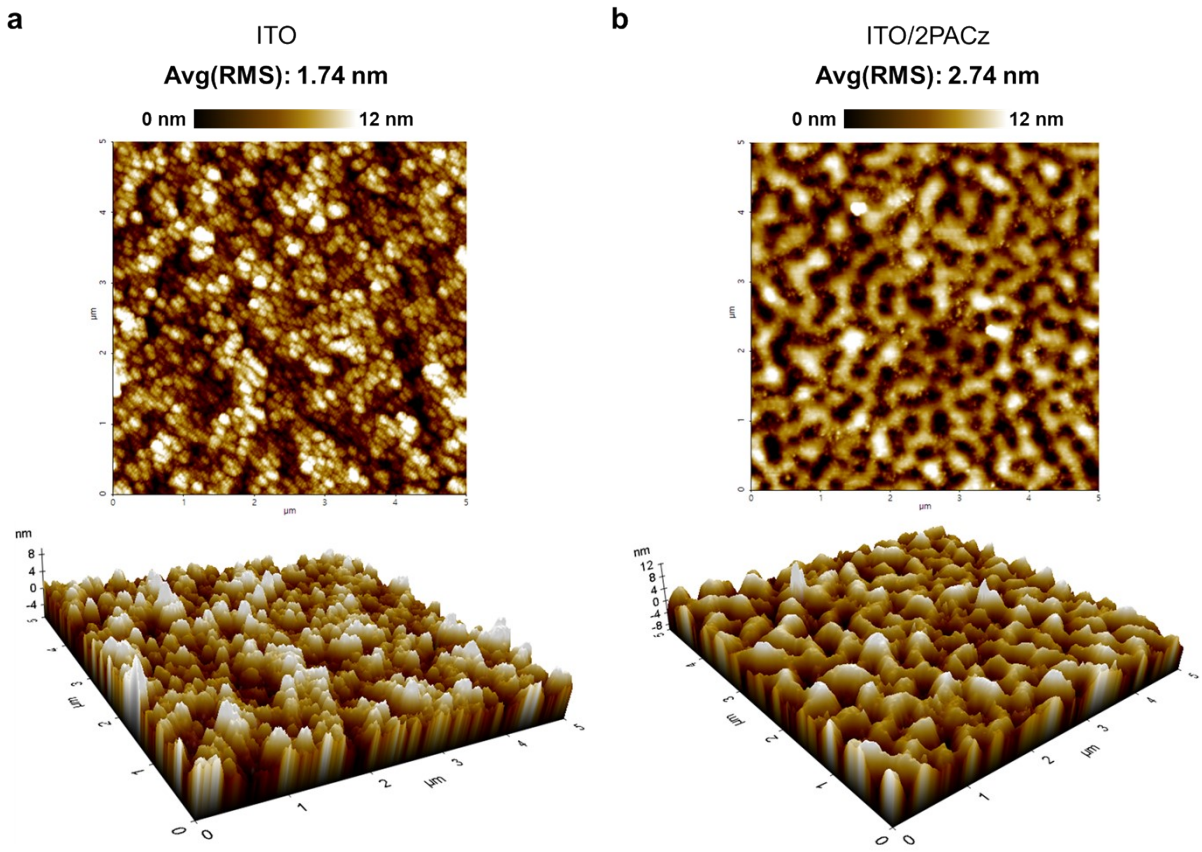

Figure S9. Topography and 3D AFM images of (a) glass/ITO and (b) ITO/2PACz surfaces.

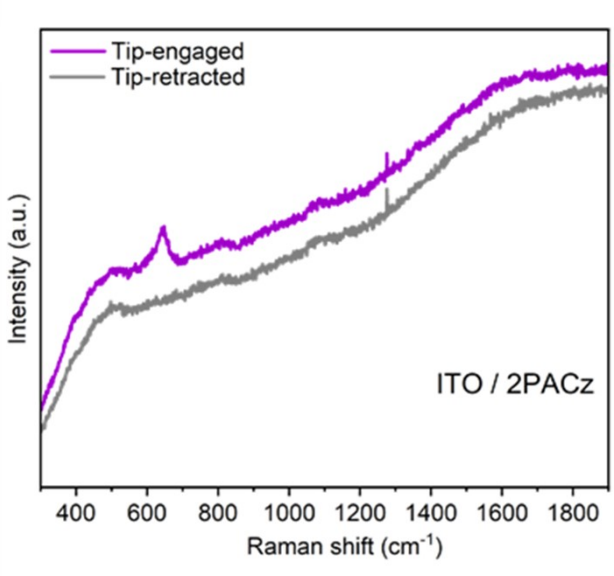

Figure S10. Tip-engaged and tip-retracted (few-nm) TERS of ITO/2PACz sample, showing the peak in 620–660 cm^{-1} region.

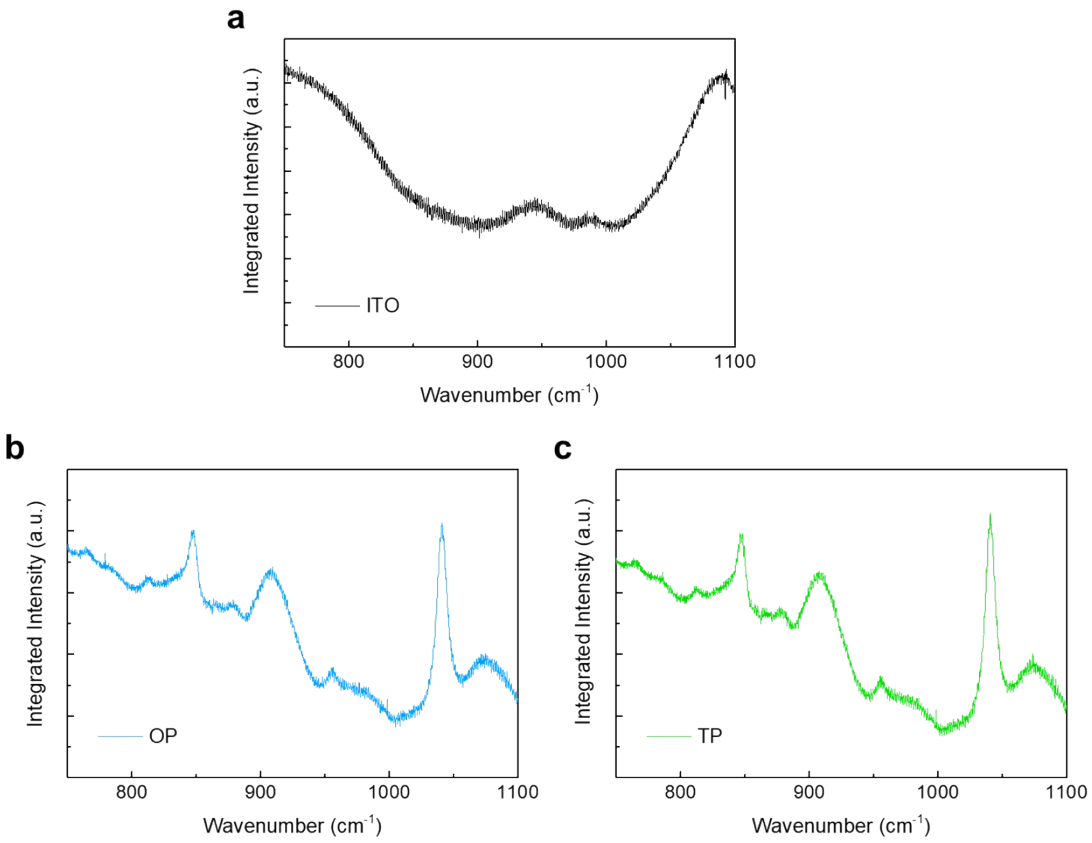

Figure S11. Far-field Raman mapping full spectrum (750–1100 cm^{-1}): (a) glass/ITO reference, peel-off SAM surface at (b) ITO/2PACz/OP and (c) ITO/2PACz/TP.

Supplementary notes: The absence of clear SAM-specific signals in TERS can be rationalized by the fact that near-field enhancement at the metal tip apex strongly amplifies vibrational modes of the conductive ITO substrate, producing the dominant 620–660 cm^{-1} response. In contrast, spectral features in the higher-frequency region (800–1200 cm^{-1}), associated with the anchoring groups of SAM, show intrinsically weaker Raman cross-sections and limited out-of-plane polarizability, resulting in minimal near-field amplification and their signals being masked by the stronger ITO contribution. Far-field Raman mapping, however, enables detection of these weaker modes and thus direct visualization of SAM desorption at the buried interface by averaging over larger sample area.

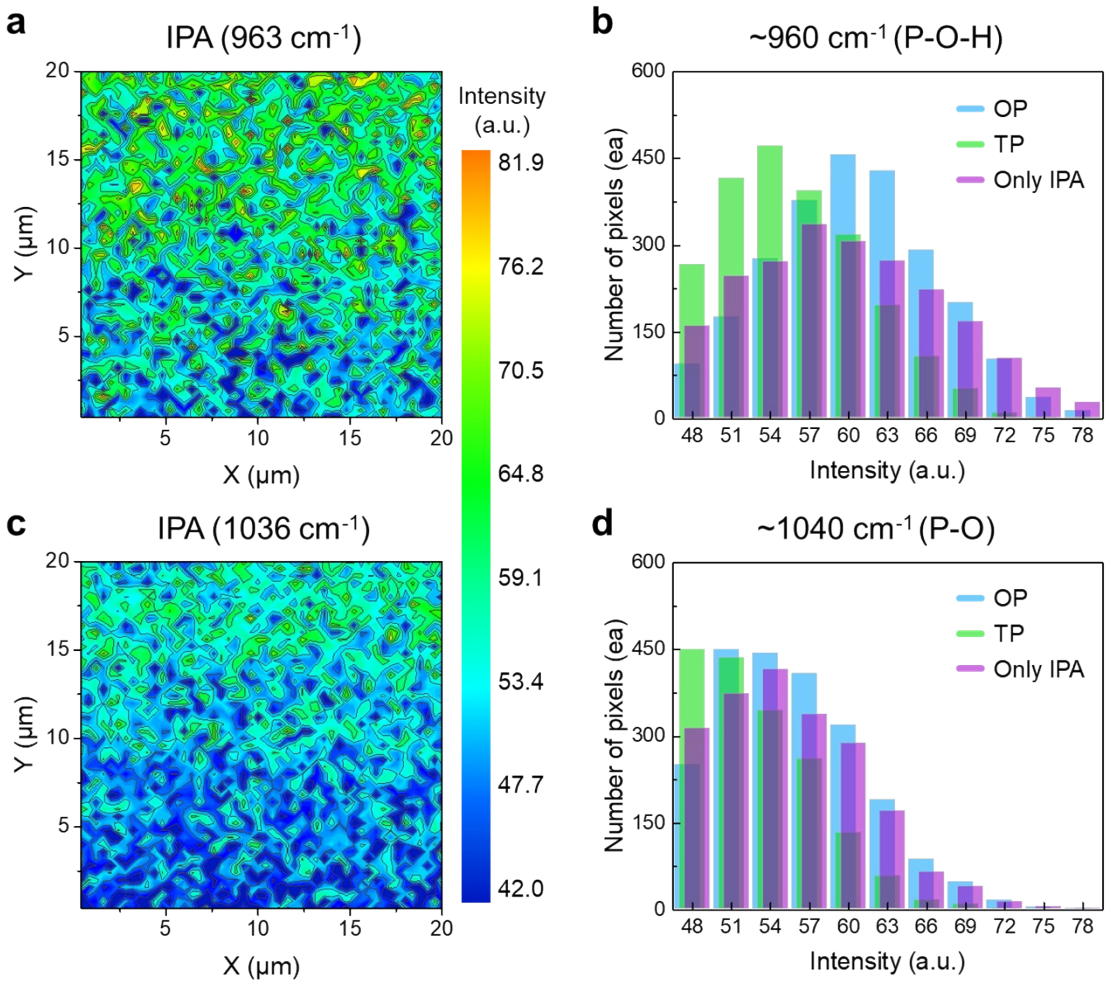

Figure S12. Far-field Raman intensity maps of the (a) P–O–H stretch (963 cm^{-1}) and (c) P–O stretch (1036 cm^{-1}) on the SAM surface of peel-off ITO/2PACz/PbI_2 substrate after exposure to IPA solvent only. Quantitative histograms of Raman intensity clusters for the SAM anchoring groups at the (b) P–O–H and (d) P–O stretching modes, extracted from the corresponding Raman maps, comparing OP, TP and IPA-only treated samples.

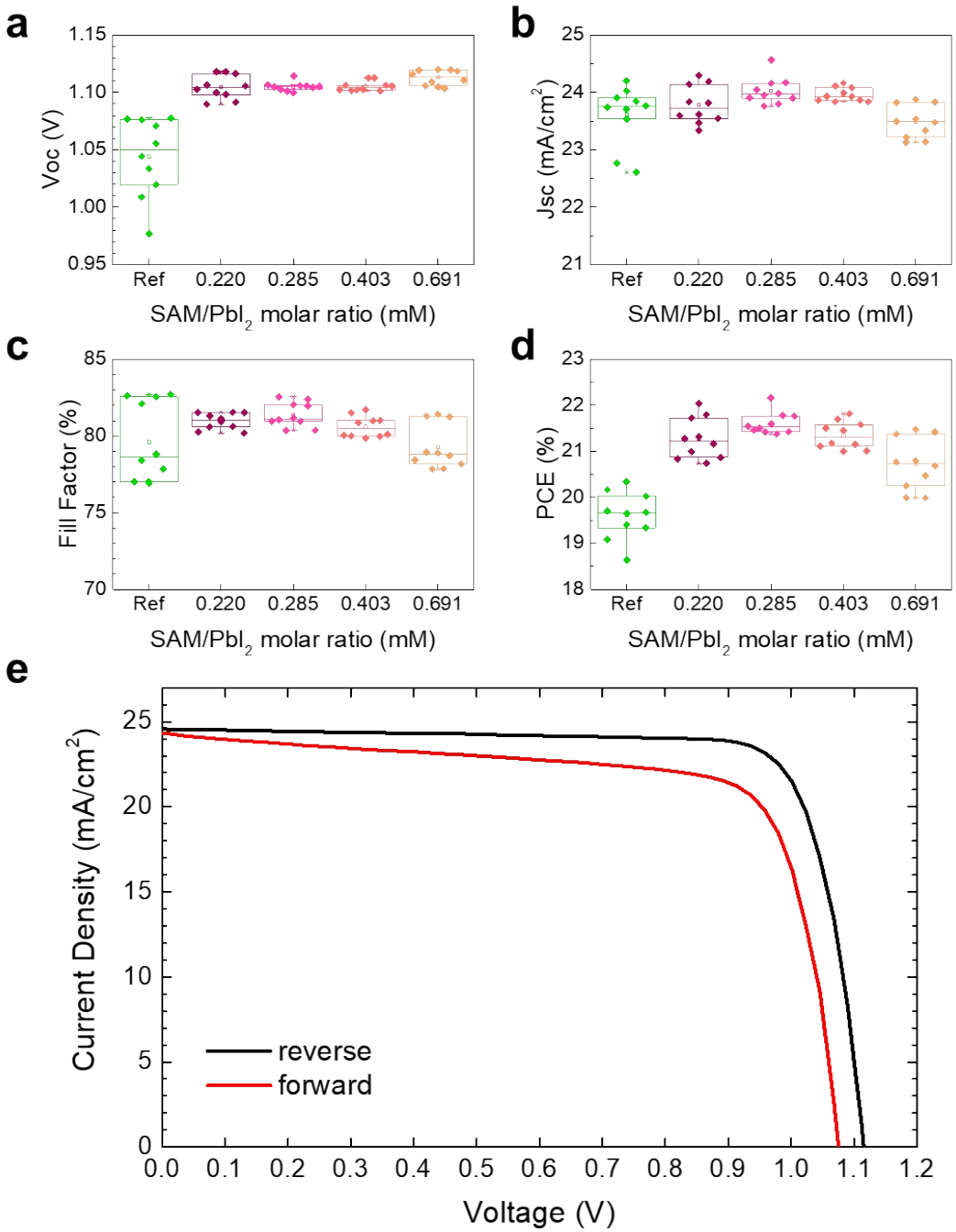

Figure S13. (a–d) *J–V* parameters of PSCs using MP and (e) *J–V* curves of PSCs for champion MP device (black: reverse scan, red: forward scan).

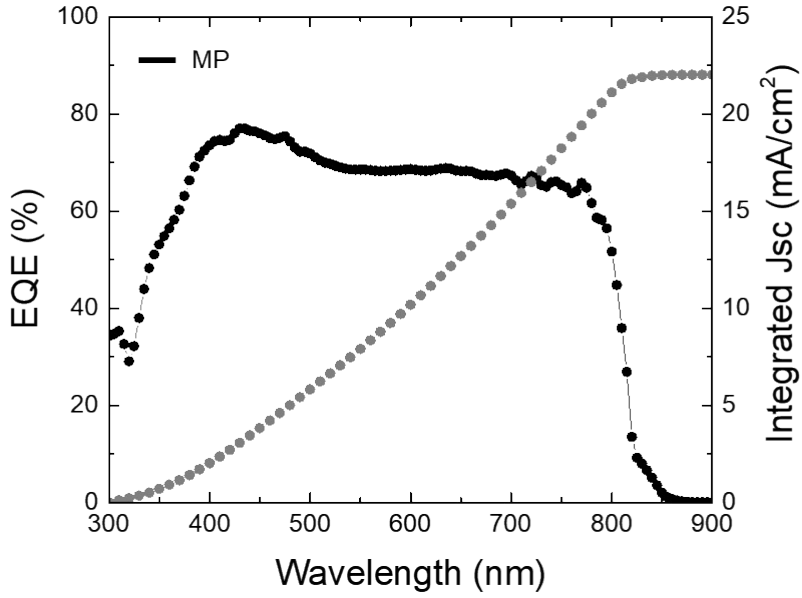

Figure S14. External quantum efficiency (EQE) spectrum and accumulated integrated J_{SC} of the optimized device with MP film.

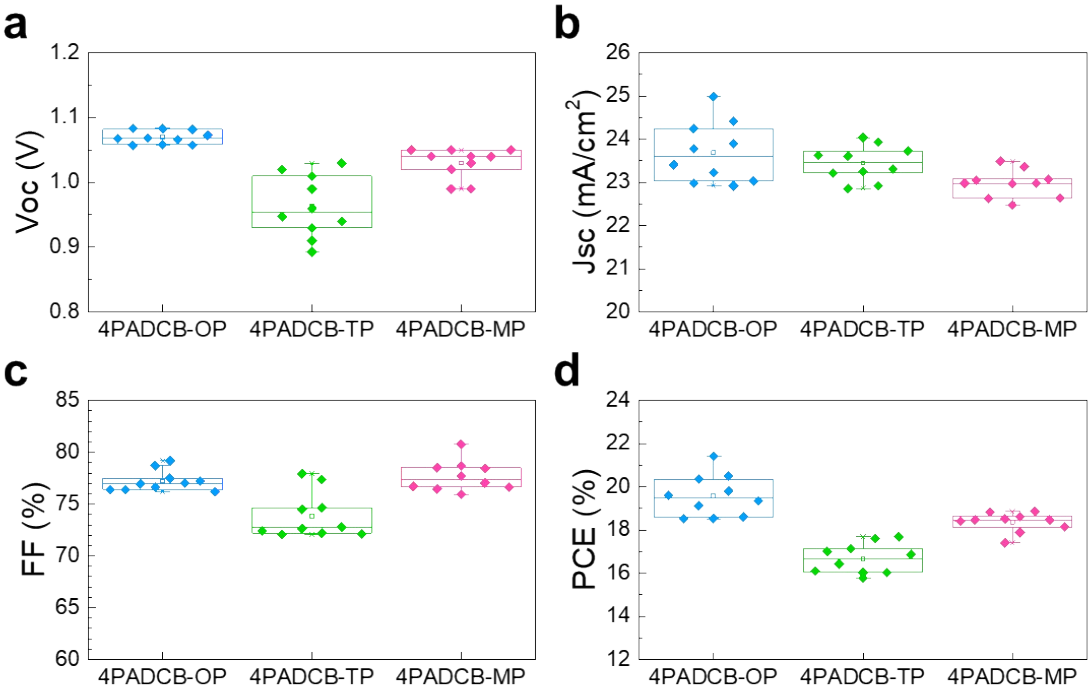

Figure S15. *J–V* parameters of inverted PSCs using 4PADCB as the HTL fabricated by the OP (blue), TP (green) and MP (pink) processes.

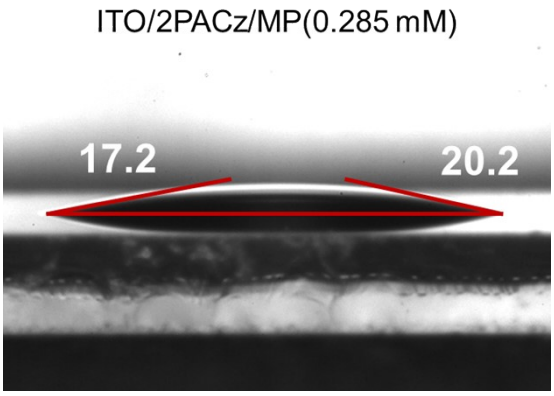

Figure S16. Contact angles measurement of MP solution on ITO/2PACz substrate.

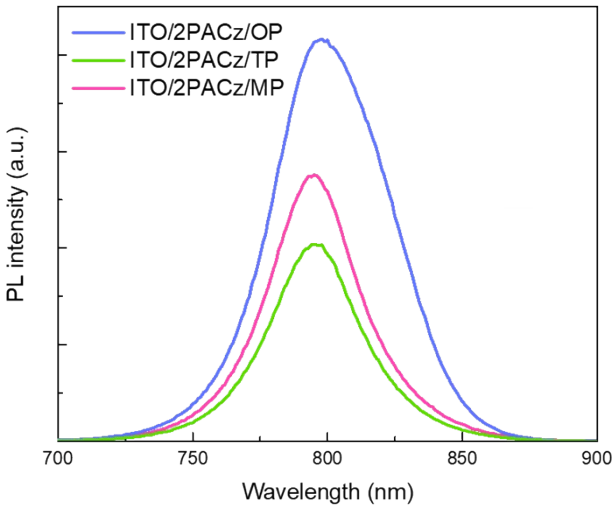

Figure S17. Comparison of steady-state PL spectra of ITO/2PACz/perovskite (OP, TP, MP).

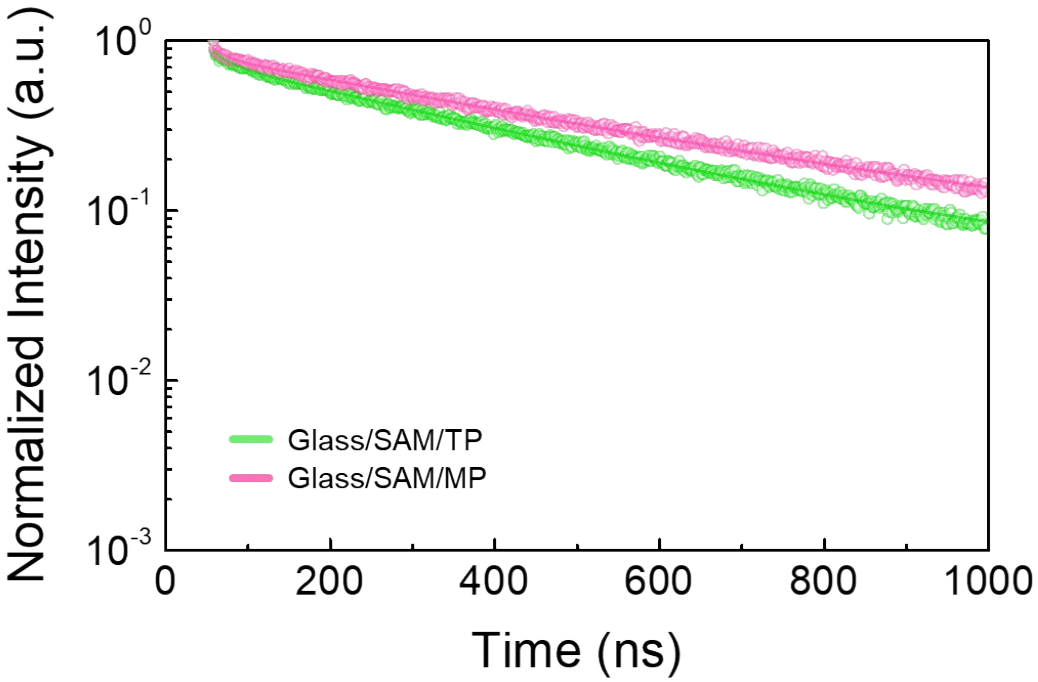

Figure S18. TRPL decay spectra of perovskite films prepared on insulating glass/SAM substrates using TP and MP.

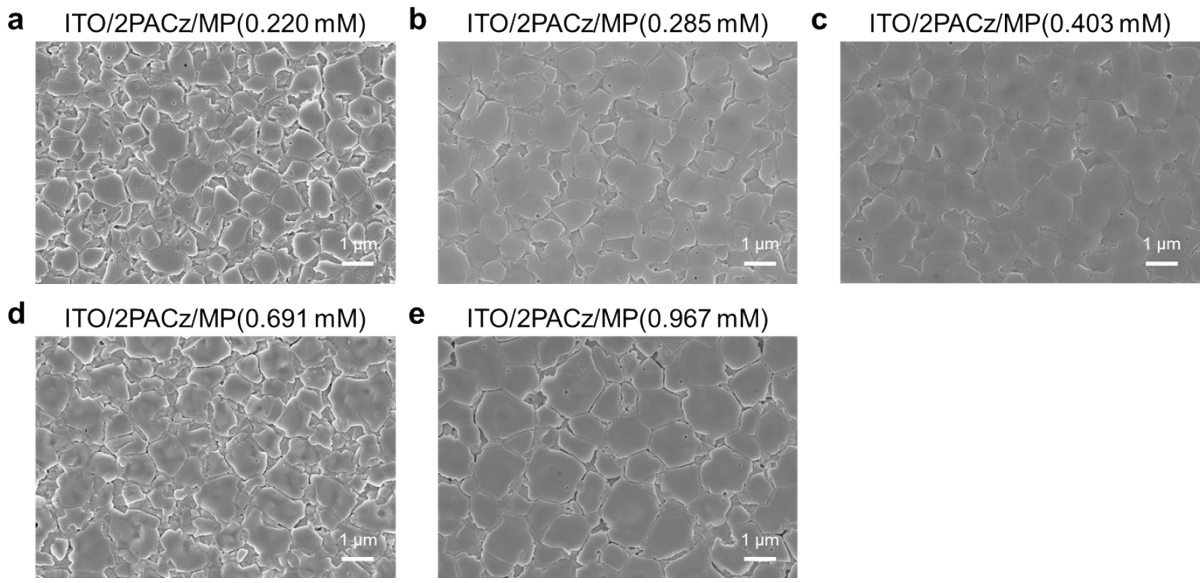

Figure S19. Top-view SEM images of the MP surfaces fabricated with different 2PACz concentrations: (a) 0.220 mM, (b) 0.285 mM, (c) 0.403 mM, (d) 0.691 mM, (e) 0.967 mM. Scale bar: 1 μm.

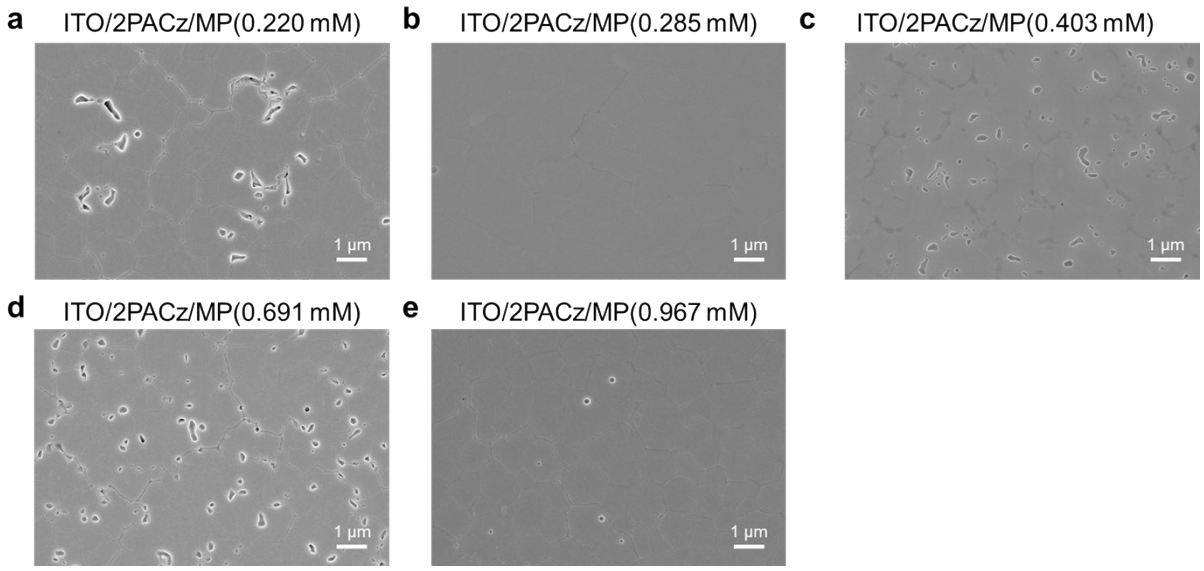

Figure S20. SEM images of the peel-off MP bottom surfaces fabricated with different 2PACz concentrations: (a) 0.220 mM, (b) 0.285 mM, (c) 0.403 mM, (d) 0.691 mM, (e) 0.967 mM. Scale bar: 1 μm.

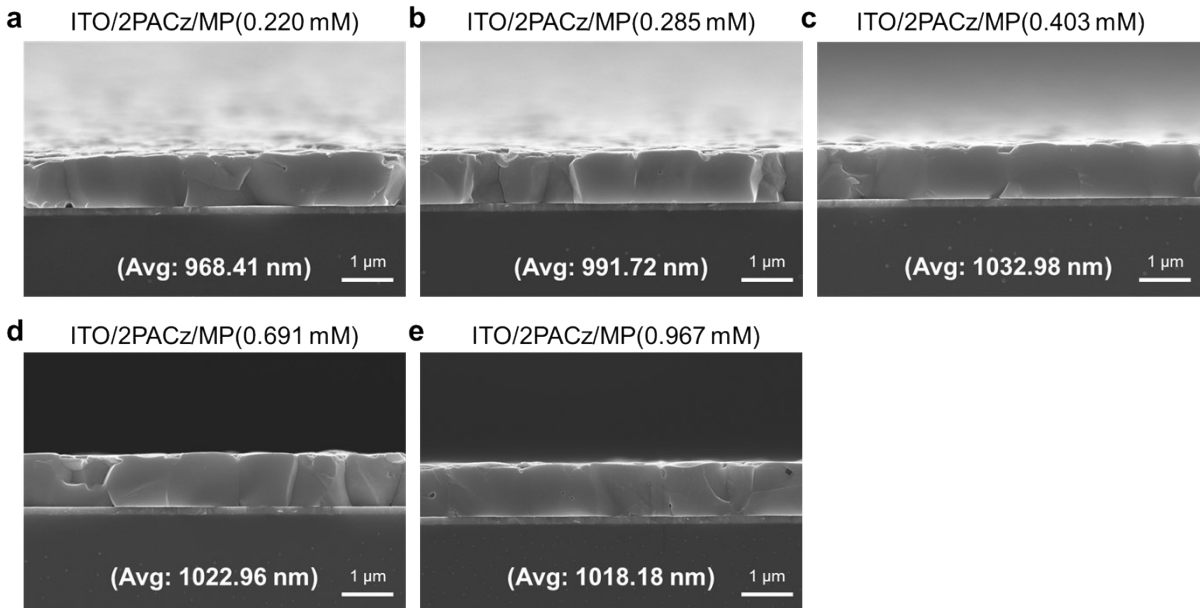

Figure S21. Cross-sectional SEM images of MP films fabricated with different 2PACz concentrations: (a) 0.220 mM, (b) 0.285 mM, (c) 0.403 mM, (d) 0.691 mM, (e) 0.967 mM. Scale bar: 1 μm.

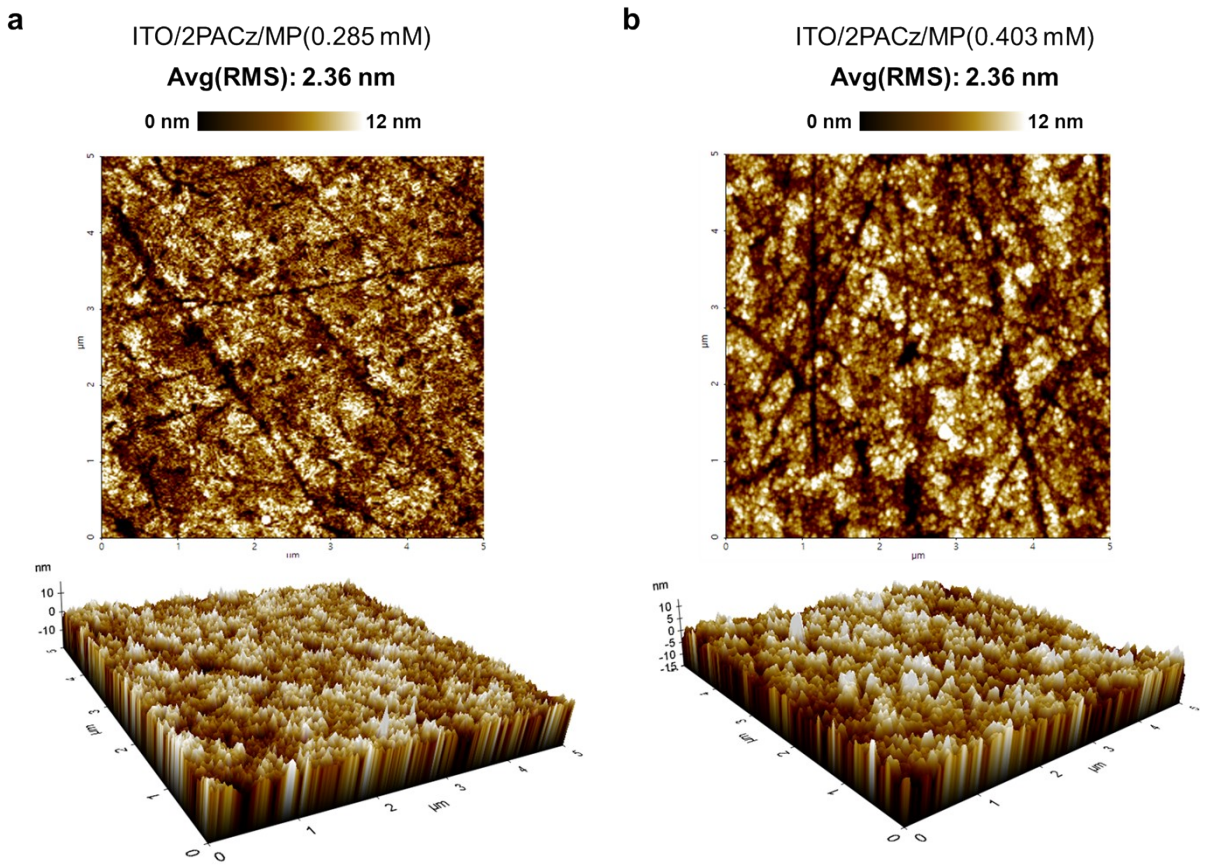

Figure S22. Topography and 3D AFM images of the peel-off SAM surfaces in MP films with different 2PACz concentration: (a) 0.285 mM, (b) 0.403 mM.

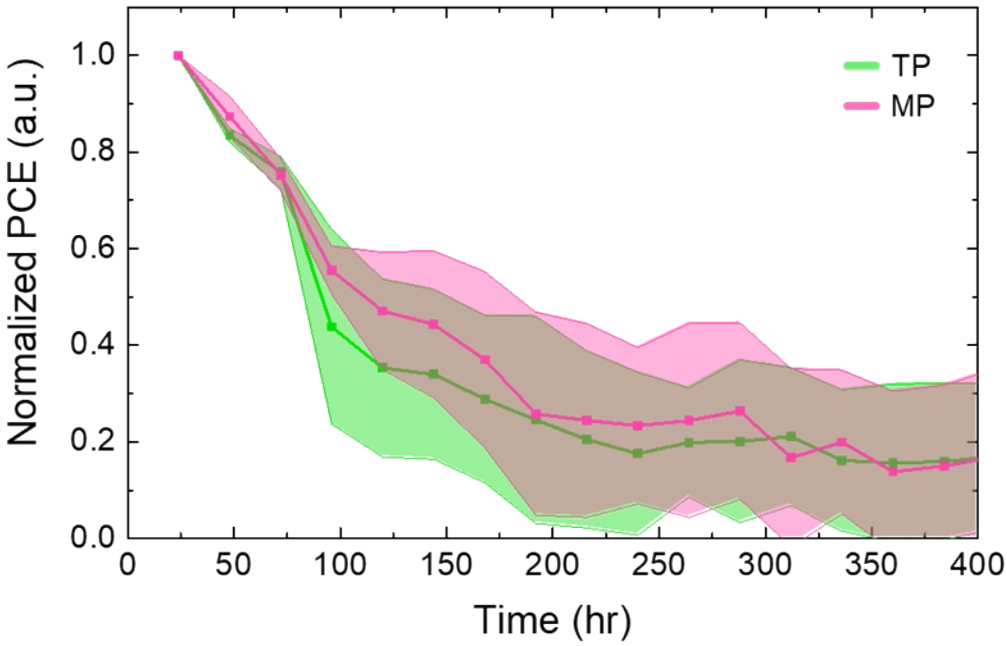

Figure S23. The light soaking stability of the encapsulated inverted PSCs fabricated by the TP and MP processes.